Draft version August 5, 2014
Preprint typeset using LaTeX style emulateapj v. 5/2/11

arXiv:1408.0750v1 [astro-ph.GA] 4 Aug 2014

INTERMEDIATE-AGE GLOBULAR CLUSTERS IN FOUR GALAXY MERGER REMNANTS

Gelys Trancho
Giant Magellan Telescope Organization, 251 S. Lake Avenue, Pasadena, CA 91101, USA, and
Carnegie Observatories, 813 Santa Barbara Street, Pasadena, CA 91101, USA

Bryan W. Miller
Gemini Observatory, Casilla 603, La Serena, Chile

François Schweizer
Carnegie Observatories, 813 Santa Barbara Street, Pasadena, CA 91101, USA

Daniel P. Burdett
The University of Adelaide, South Australia 5005, Australia

and

David Palamara
Monash University, Clayton, Victoria 3800, Australia

Draft version August 5, 2014

ABSTRACT

We present the results of combining *Hubble Space Telescope* optical photometry with ground-based K_s-band photometry from the Gemini imagers NIRI and FLAMINGOS-I to study the globular-cluster populations in four early-type galaxies that are candidate remnants of recent mergers (NGC 1700, NGC 2865, NGC 4382, and NGC 7727). These galaxies were chosen based on their blue colors and fine structure, such as shells and ripples that are indicative of past interactions. We fit the combined VIK_s globular-cluster data with simple toy models of mixed cluster populations that contain three subpopulations of different age and metallicity. The fits, done via Chi-square mapping of the parameter space, yield clear evidence for the presence of intermediate-age clusters in each galaxy. We find that the ages of $\sim$1 – 2 Gyr for these globular-cluster subpopulations are consistent with the previously estimated merger ages for the host galaxies.

Subject headings: galaxies: individual (NGC 1700, NGC 2865, NGC 4382, NGC 7727) — galaxies: interactions — galaxies: star clusters: general

1. INTRODUCTION

Studies of globular cluster (GC) systems play a critical role in our understanding of galaxy formation. Until two decades ago it was thought that all GCs were old, and this shaped our view of how galaxies, especially elliptical galaxies, formed (see Harris 1991). Imaging with the *Hubble Space Telescope (HST)* then revealed that young compact star clusters form copiously in galaxy mergers (Whitmore et al. 1993; Miller et al. 1997; Zepf et al. 1999), a fact that supports theories in which giant elliptical galaxies are formed through mergers of spirals (Schweizer 1987; Ashman & Zepf 1992).

However, the formation and evolution of GC systems is still not well understood. We should be able to observe how GC systems evolve from the very young systems with power-law luminosity functions into old systems with log-normal luminosity functions, such as are observed in typical elliptical galaxies. These observations would greatly clarify exactly which processes (shocking, evaporation, dynamical friction; e.g., Fall & Zhang 2001) are important in the evolution of star cluster systems.

Finding intermediate-age GC populations in elliptical galaxies has been difficult. Spectroscopy is often thought to be a relatively accurate method for measuring cluster ages and metallicities. However, in practice spectroscopy is very time consuming, even for 8 m-class telescopes, leaving only the brightest GCs open to such analyses. Strader et al. (2003) spent 9.3 hours observing nine GC candidates in the E5 galaxy NGC 3610 with Keck, and found only one young GC.

The majority of candidate GCs in galaxies identified via morphology and color to be intermediate-age merger remnants are too faint for spectroscopic study. Photometric studies have also had limited success, partly because most have been done only at optical wavelengths (specifically, in the V and I passbands). The problem is that the $V-I$ colors of metal-rich GCs with ages of 1–3 Gyr overlap with the colors of $\sim$13 Gyr old metal-poor GCs, resulting in an age-metallicity degeneracy (Whitmore et al. 1997, esp. Fig. 15). Fortunately, the combination of optical and near-infrared (NIR) photometry can break this age–metallicity degeneracy. This is because optical-to-NIR indices are sensitive to metallicity, but only weakly dependent on age (e.g., Kissler-Patig 2000; Puzia et al. 2002). Physically this works because in older stellar populations the V-band predominantly samples the light of stars near the turn-off, while the K_s-band is more sensitive to cooler stars on the giant branch.

gtrancho@gmto.org

The color of the giant branch is metallicity-dependent, so the index $V-K_s$ is primarily a metallicity indicator. Thus, we can lift the age–metallicity degeneracy by plotting the locations of Simple Stellar Populations (SSP) in a color–color diagram, specifically $V-I$ vs. $V-K_s$.

2. OBSERVATIONS AND REDUCTIONS

2.1. *Sample Selection*

The four early-type galaxies NGC 1700, NGC 2865, NGC 4382, and NGC 7727 were selected based on their tidal fine-structure content, blue *UBV* colors, and enhanced Balmer absorption lines (Schweizer & Seitzer 1992; Schweizer et al. 1990). The sample spans the morphology and age gap between on-going mergers and normal elliptical galaxies.

NGC 4382 is similar to the merger remnants NGC 7252, NGC 3921, and NGC 7727, but lacks tidal tails. Its rich fine structure and distortions (see Fig. 1 in Schweizer & Seitzer 1988 and Fig. 9 in Kormendy et al. 2009) suggest that it experienced a merger 1 – 2 Gyr ago, a hypothesis strengthened by its still bluish center (Fisher et al. 1996), double-peaked nucleus (Lauer et al. 2005), and counter-rotating core (McDermid et al. 2004). It was selected specifically to bridge the age gap between ongoing mergers like NGC 4038/39 or NGC 3256 and normal old ellipticals.

The elliptical galaxies NGC 1700 and NGC 2865 both show evidence for recent interactions or mergers and are therefore candidate "young ellipticals."

NGC 1700 features boxy isophotes, a strong isophotal twist, and two broad arms or tails that have long suggested it may be the remnant of a major merger of two disk galaxies (Seitzer & Schweizer 1990, esp. Fig. 1b; Brown et al. 2000). Its kinematics supports this hypothesis: it rotates fast (Statler et al. 1996), yet features a counterrotating core with a distinctly younger stellar population (Kleineberg et al. 2011). Whitmore et al. (1997) found that its GCs are consistent with an age of $\sim$4 Gyr, but do not necessarily form a population of obviously intermediate age.

NGC 2865 features bright irregular shells, a luminous plume of material, and a faint outer loop, all suggesting that it is the remnant of a relatively recent merger (see Fig. 5 of Malin & Carter 1983 and Fig. 1 of Hau et al. 1999). This hypothesis is supported by H I gas fragments associated with the optical fine structure (Schiminovich et al. 1995), a rapidly rotating small central core with a younger stellar population and gas (Hau et al. 1999; Serra & Oosterloo 2010), and a body with unusually blue *UBV* colors. Sikkema et al. (2006) note that in a color histogram the galaxy's GCs seem to contain a subpopulation bluer than normal metal-poor GCs and, hence, likely of much younger age ($\sim$0.5 – 1 Gyr).

Finally, NGC 7727 (= VV67 = Arp 222) is so obviously tidally disturbed that it was included by both Vorontsov-Velyaminov (1959) and Arp (1966) in their catalogs of interacting galaxies. Because of its spiral-shaped tidal tails it was originally classified as a peculiar Sa galaxy (de Vaucouleurs & de Vaucouleurs 1964; Sandage & Tammann 1981), but was then reclassified as a recent merger remnant of age $\sim$1.3 Gyr by Georgakakis et al. (2000). The presence of bluish young star clusters in it was noted by Crabtree & Smecker-Hane (1994) and described in some more detail by Trancho et al. (2004).

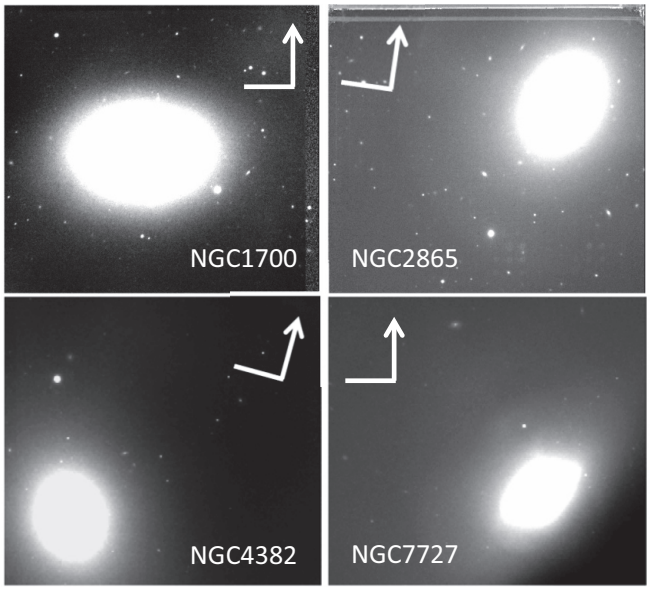

Figure 1. K_s-band images of NGC 1700, NGC 2865, and NGC 4382 obtained with NIRI, and of NGC 7727 obtained with FLAMINGOS-I. The integrated exposure times were 0.5, 0.2, 0.5, and 1.0 hours, respectively.

2.2. *Observations*

We obtained K_s-band images of the above four early-type galaxies with the Near-InfraRed Imager and Spectrometer (NIRI) on Gemini North (Hodapp et al. 2003) and with FLAMINGOS-I on Gemini South (Elston et al. 2003), with the results shown in Figure 1.

The program IDs were GN-2006B-Q-97 and GS-2002A-DD-4, respectively. We used NIRI in f/6 imaging mode, which yields an image scale of 0.″117/pixel and a field of view of $2' \times 2'$, and FLAMINGOS-I also in imaging mode, which yields a scale of 0.″078/pixel and a field of view of $2.'2 \times 2.'2$. Both instrument have similar fields of view, comparable to those of the WFPC2 and ACS cameras on *HST*.

All four galaxies were also observed with *HST* in *V* and *I* (GO-7468, PI: Schweizer), and we used unpublished photometry from that project. In the case of NGC 4382, we used the most recent photometric data published by Jordan et al. (2009).

Table 1 summarizes our observations and the data from other authors used in this study.

2.3. *Data Reduction*

The data were reduced with the Gemini/NIRI package of tasks within IRAF. Normalized flats were constructed from images taken with the Gemini calibration unit. Flat-field images with the IR lamp on and off allowed separation of the instrumental thermal signature from the sensitivity response.

The near-IR sky level and structure varies on time scales of a few minutes. To account for such variations we used a dither pattern in our imaging sequences, which provided blank fields close enough in time to derive the sky levels reliably.

Table 1
Summary of galaxy observations and data

Galaxy	Distance[a]	Filter	Telescope/Instrument	Author
NGC 1700	52	V, I	*HST*/WFPC2	Whitmore et al. (1997)
		K_s	Gemini/NIRI	This Paper
NGC 2865	35	V, I	*HST*/WFPC2	Schweizer (Cycle 7)[b]
		K_s	Gemini/NIRI	This Paper
NGC 4382	16	V, I[c]	*HST*/ACS	Jordan et al. (2009)
		K_s	Gemini/NIRI	This Paper
NGC 7727	26	V, I	HST/WFPC2	Trancho et al. (2004)
		K_s	Gemini/FLAMINGOS-I	This Paper

[a] Distance (in Mpc) based on recession velocity relative to the Local Group and $H_0 = 73$ km s^{-1} Mpc^{-1} (Freedman & Madore 2010).
[b] Unpublished data.
[c] The data were originally in the passbands g, z and were transformed to V, I using equations by Peng et al. (2006, Eqs. (1) and (2)).

Some of the NIRI frames contain an electronic pattern visible as vertical striping with a period of eight columns and not always present in all quadrants. Before including the affected frames in our image processing list we used the stand-alone python routine *nirinoise.py* which almost perfectly removed the striping. The same image reduction steps were applied to the standard star observations as well.

All reduced science and standard star exposures of the corresponding nights were registered to a common coordinate system with the task *imcoadd*, based on geometric solutions obtained with the task *geomap* for NIRI. The final K_s science image for each galaxy was derived by averaging individual images, scaled to the galaxy image from the most photometric night, with the IRAF task *imcombine*.

3. PHOTOMETRY

3.1. *Source Detection*

To detect as many GCs as possible from our K_s-band images and match them with existing *HST* photometry, we first created a model image of each galaxy with the tasks *ellipse* and *bmodel* of the *isophote* package in IRAF. This model image was then subtracted from the original combined galaxy image. This procedure facilitated the uniform detection of point sources at a detection threshold of 3σ above the background, using the task *daofind* of the *daophot* package. Figure 2 shows an example of this technique.

3.2. *Photometric Calibration*

The photometry of the candidate GCs in our sample of merger remnants was calibrated to K_s on the standard system via 14″-aperture photometry matching that used in the 2MASS survey. This method was chosen because the standard stars observed with Gemini indicated significant variability in the zero point during our observations. The conditions that these galaxies were observed under were IQ70 and, therefore, not guaranteed to be photometric. The FLAMINGOS-I observations, on the other hand, showed a high level of agreement with the calibration via the 2MASS stars; coincidently, this night had very good photometric conditions.

3.3. *GC Selection*

We matched the optical *HST* observations (already reduced and calibrated) with our infrared GC candidates using the IRAF tasks *geomap* and *geotran*. The brightest common objects in both images served as points of reference.

3.4. *Completeness Correction*

The initial selection of GC candidates was largely based on applying color limits to the objects identified in the V, I, and K_s images. However, it was expected that this method alone would prove insufficient to remove contaminants such as background galaxies and foreground stars. Therefore, the photometric completeness of the data was determined, and a visual inspection of each GC candidate was performed.

Since this study utilized space-based V and I images, but ground-based K_s images, it was expected that the K_s images would set the completeness limit for the photometric data. Hence, a set of completeness curves were generated from the K_s images obtained with NIRI and FLAMINGOS-I for each galaxy. These curves were created through the addition of artificial cluster images to each galaxy image, using the DAOPHOT task *addstar*. For each of the galaxies NGC 1700, NGC 2865, and NGC 7727, 100,000 artificial cluster images ranging from 15 to 25 magnitudes were added, with no more than 100 clusters added to any one image to prevent overcrowding. In the case of NGC 4382, which exhibits an already relatively crowded field of point sources, only 50 artificial clusters were added to each image, effectively halving the total number of artificial clusters studied. The DAOPHOT tasks *daofind* and *phot* were then used to attempt to recover these artificial clusters, and to perform photometry on them. This process was repeated for background values of 25, 65, 85, 125, and 250 counts per pixel.

This process allowed us to generate two kinds of completeness curves for the GCs of each galaxy. Curves of the first kind represented the fraction of artificial clusters that were successfully recovered by the task *daofind*. Completeness curves of the second kind represented the fraction of artificial clusters that were not only successfully recovered by *daofind*, but that also returned a photometric magnitude within acceptable limits via the task *phot*. There were two of these limits: the returned photometric magnitude was required to have an error of <0.3 mag and was also required to be within 0.5 mag of the magnitude of the input artificial-cluster image.

A smoothed curve based on the completeness func-

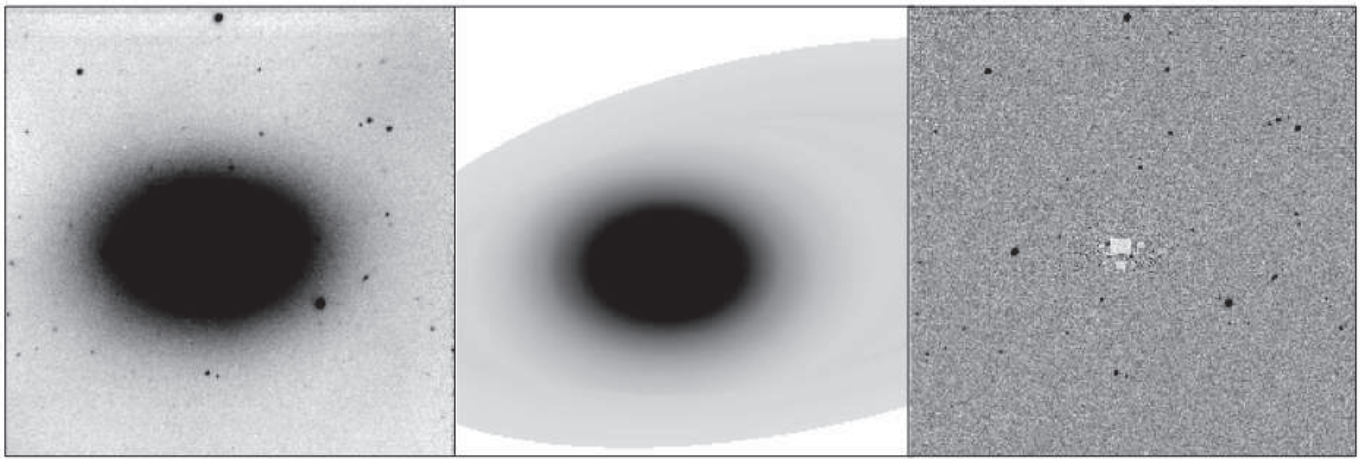

Figure 2. From left to right: K_s-band image of NGC 1700, galaxy model of NGC 1700, and model-subtracted image.

tion given in Fleming et al. (1995) was fit to each set of completeness curves generated. The two parameters returned by this fitting procedure were the 50% completeness limit, $K_{s,\rm lim}$ (expressed in magnitudes), and a steepness parameter α. Table 2 presents for each galaxy and background value the two fit parameters derived, both for the first kind of completeness curves (subscript "fnd" for "found") and for the second kind (subscript "acc" for "accepted").

As mentioned above, several completeness curves were generated for each galaxy in order to determine the stability of the photometric completeness limit over a range of background values. Given that the background varied considerably over any one image, particularly across the center of the galaxy, such stability was essential. Indeed, the variance in background over each image considerably affected the point-spread functions (PSFs) that we attempted to construct. In order to negate this effect, the final PSFs that were used in the artificial cluster addition were generated from background-subtracted GC images, as illustrated in Figure 3. These background-subtracted GC images were created using a 15 × 15-pixel median subtraction.

¿From the results presented in Table 2 it is evident that—although the steepness of the completeness curves did vary—the 50% completeness limit was exceptionally stable over the range of background values investigated. Therefore, we were able to use a single completeness limit for each image, despite the fact that the background values varied dramatically across the cores of the galaxies.

3.4.1. *NGC 1700*

Figure 4 shows the completeness curve derived for GCs in NGC 1700 (shown for accepted artificial clusters only). As Table 2 details, the 50% K_s completeness limits were $K_{s,\rm lim} = 21.90 - 21.91$ for both the recovered and the accepted clusters at all background levels. Hence, it is evident that photometric errors do not play a significant role in setting the depth of completeness in this case. Rather, the completeness is limited primarily by our ability to detect the clusters.

3.4.2. *NGC 2865*

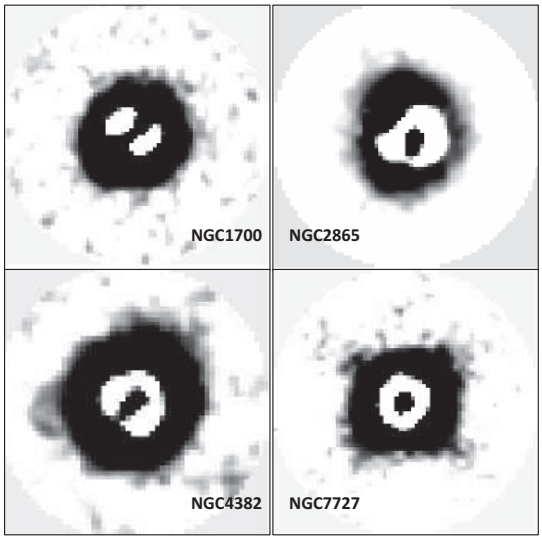

Figure 3. PSFs generated from the median background-subtracted images of NGC 1700, NGC 2865, NGC 4382, and NGC 7727. The field of view is $7.8'' \times 7.8''$ for each panel.

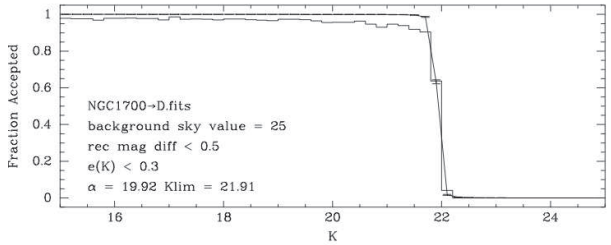

Figure 4. Completeness curve for NGC 1700 derived from artificial cluster addition. The histogram shows the fraction of clusters recovered to within acceptable error and magnitude limits, while the smooth curve indicates the fitted completeness function.

Figure 5 shows the completeness curve derived for GCs in NGC 2865. In this galaxy, the 50% completeness limits were $K_{s,\rm lim} = 21.51 - 21.52$ for both the recovered and the accepted artificial clusters. As in the case of NGC 1700, the very small range of these values indicates that the completeness in K_s was limited by our ability

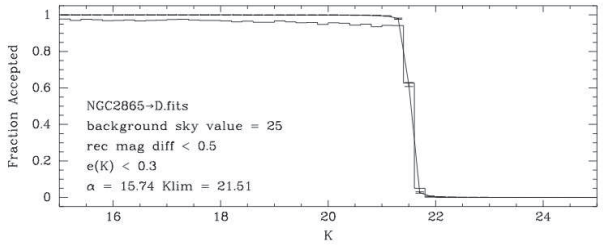

Figure 5. Completeness curve for NGC 2865 derived from artificial cluster addition. The histogram shows the fraction of clusters recovered to within acceptable error and magnitude limits, while the smooth curve indicates the fitted completeness function.

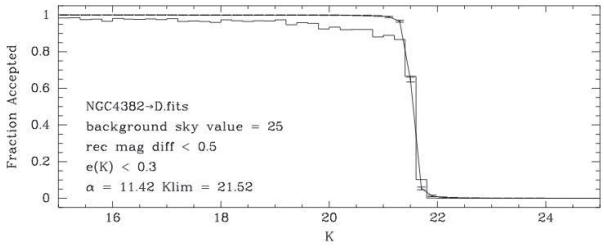

Figure 6. Completeness curve for NGC 4382 derived from artificial cluster addition. The histogram shows the fraction of clusters recovered to within acceptable error and magnitude limits, while the smooth curve indicates the fitted completeness function.

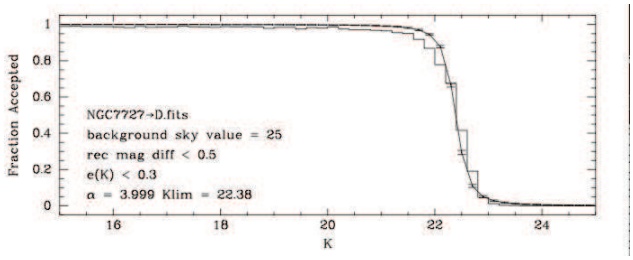

Figure 7. Completeness curve for NGC 7727 derived from artificial cluster addition. The histogram shows the fraction of clusters recovered to within acceptable error and magnitude limits, while the smooth curve indicates the fitted completeness function.

to detect the clusters rather than by photometric errors.

3.4.3. *NGC 4382*

Figure 6 shows the completeness curve derived for GCs in NGC 4382. Again, the K_s 50% completeness limits are similar for the recovered and accepted curves, though with wider scatter than in NGC 1700 and NGC 2865 and with a 0.06 mag difference between the two mean values (see Table 2).

3.4.4. *NGC 7727*

Figure 7 shows the completeness curve derived for GCs in NGC 7727.

As Table 2 details, the various K_s 50% completeness limits scatter more and show a significant systematic difference of 0.09 mag between the recovered artificial clusters (mean $K_{s,\mathrm{lim,fnd}} = 22.46$) and the accepted clusters (mean $K_{s,\mathrm{lim,acc}} = 22.37$). Notice that these limits for the NGC 7727 GCs are more than 0.5 mag fainter than the limits for GCs in the other three galaxies, which is not surprising given that the K_s images of NGC 7727 were obtained with FLAMINGOS-I on a night of particularly good seeing. It is because of these fainter limits that the photometric errors are more influential in NGC 7727 than in the other three galaxies.

Nevertheless, we adopted the single value of $K_{s,\mathrm{lim,acc}} = 22.37$ as our acceptance criterion for candidate GCs in NGC 7727.

Table 2
Summary of the parameters for the completeness curves for each galaxy.

Galaxy NGC	Sky Value (counts)	$K_{s,\mathrm{lim,fnd}}$[a] (mag)	α_{fnd}[b]	$K_{s,\mathrm{lim,acc}}$[a] (mag)	α_{acc}[b]
1700	25	21.91	22.05	21.90	19.27
1700	55	21.91	15.74	21.90	12.84
1700	85	21.91	21.19	21.90	9.17
1700	125	21.91	18.41	21.90	18.97
1700	250	21.91	17.62	21.90	16.33
2865	25	21.52	16.00	21.51	15.10
2865	55	21.52	11.81	21.51	12.81
2865	85	21.51	16.67	21.51	13.33
2865	125	21.52	15.39	21.51	7.09
2865	250	21.52	14.63	21.51	8.37
4382	25	21.55	11.57	21.51	10.55
4382	55	21.56	11.18	21.46	3.68
4382	85	21.55	11.87	21.51	14.11
4382	125	21.57	10.49	21.51	10.03
4382	250	21.54	13.03	21.47	4.01
7727	25	22.46	3.93	22.38	3.99
7727	55	22.45	3.76	22.37	4.44
7727	85	22.46	4.26	22.38	3.81
7727	125	22.46	3.94	22.37	3.55
7727	250	22.45	3.96	22.35	3.55

[a] 50% K_s completeness limit.
[b] Curve fitting parameter (Fleming et al. 1995) governing the slope of the fit.

Table 3
Summary of globular-cluster candidates removed during each correction

Galaxy NGC	Initial GC Candidates	Removed via Completeness	Removed via Visual Inspection	Final GC Candidates
1700	45	6	13	26
2865	65	2	20	43
4382	65	3	2	60
7727	31	0	9	22

3.5. *Further Corrections*

In addition to the completeness corrections we performed a visual examination of each GC candidate, using the IRAF task *imexam* to further remove any contaminants such as background galaxies. Candidates were dropped if their shape was particularly elliptical and/or if the counts per pixel within the object were well below those of the other candidates. Table 3 gives a summary of the GC candidate corrections applied for each GC system. Figures 8 and 9 show the resulting color–color and color–magnitude diagrams for the GC systems of NGC 2865 and NGC 7727, respectively.

4. FITTING TO SSP MODELS

In order to constrain the age of the merger event for each of the four galaxies, the ages of their GC subpopulations were determined. Specifically, we assumed that

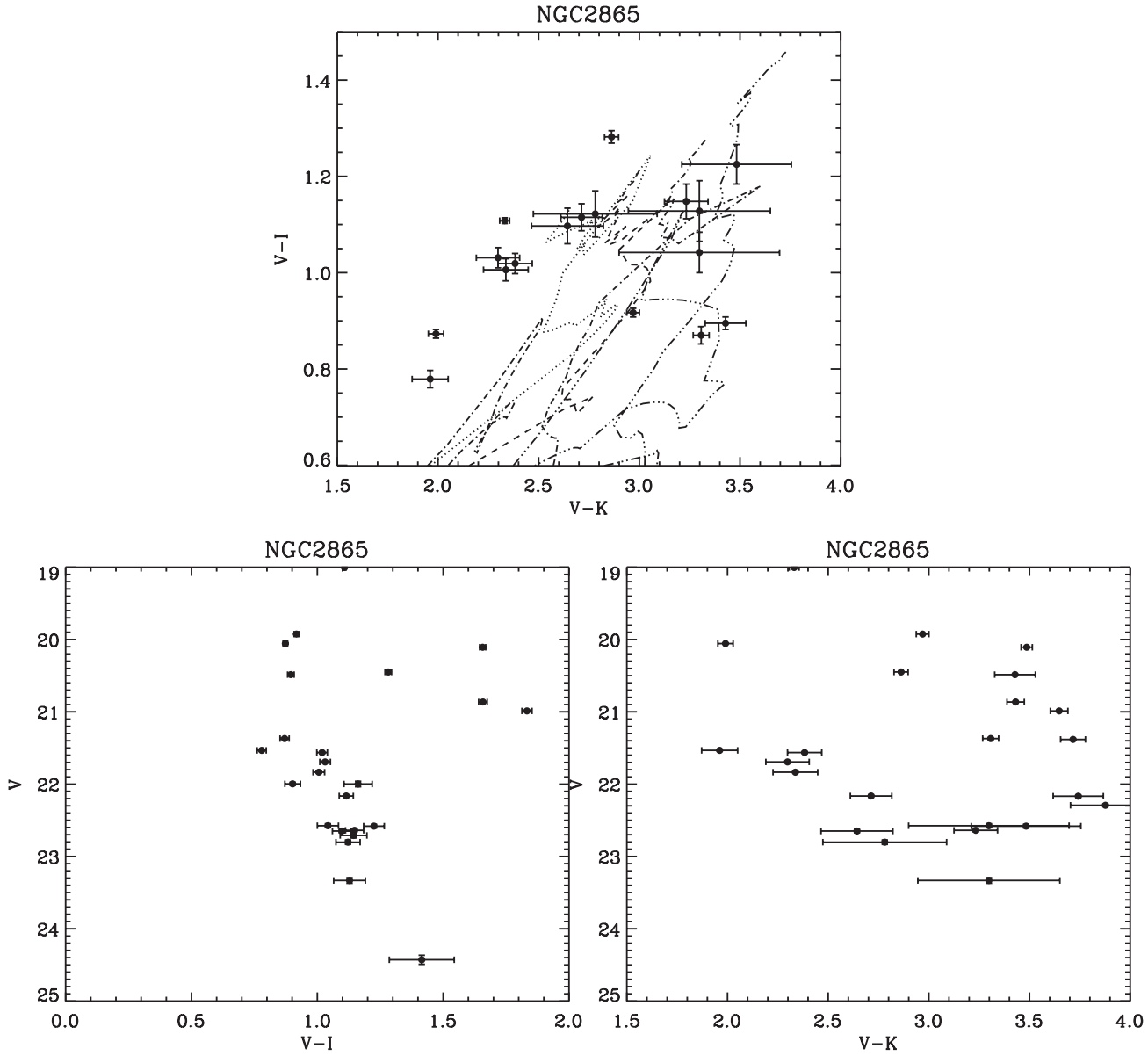

Figure 8. Color–magnitude and color–color diagrams for GCs of NGC 2865.

the parameters of the youngest subpopulation may be associated with the most recent major star-formation episode—the galaxy-merger event itself.

Conventional studies of GC ages and metallicities are often based on optical-to-NIR color–magnitude diagrams such as, e.g., the V vs $V-I$ diagram. However, such diagrams suffer from an inherent age–metallicity degeneracy (e.g., Worthey 1999), and it is often difficult to disentangle age and metallicity without additional detailed spectra.

In an effort to break—or at least partly lift—this degeneracy, we use VIK_s color–color diagrams (specifically $V-I$ vs $V-K_s$) and interpret the measured GC colors via the SSP models generated by Charlot & Bruzual (2007, private communication, hereafter CB07; see Bruzual & Charlot 2003 and Bruzual 2007 for published models and details).

The fitting algorithm used to match the models to our data is briefly described below and closely follows the method and algorithm used by Hempel & Kissler-Patig (2004). We also present the results of our efforts to verify the technique.

4.1. *Methodology*

Our principal goal was to identify the possible presence of multiple subpopulations among the GCs of our sample galaxies and to estimate their ages, based on simple assumptions about their metallicities.

We assume that there are three predominant cluster subpopulations of interest: one consisting of ∼13 Gyr old metal-poor GCs, a second one of also old (>10 Gyr) metal-rich GCs, and a third one of younger, intermediate-age metal-rich GCs. The universal old metal-poor subpopulation is present in all major galax-

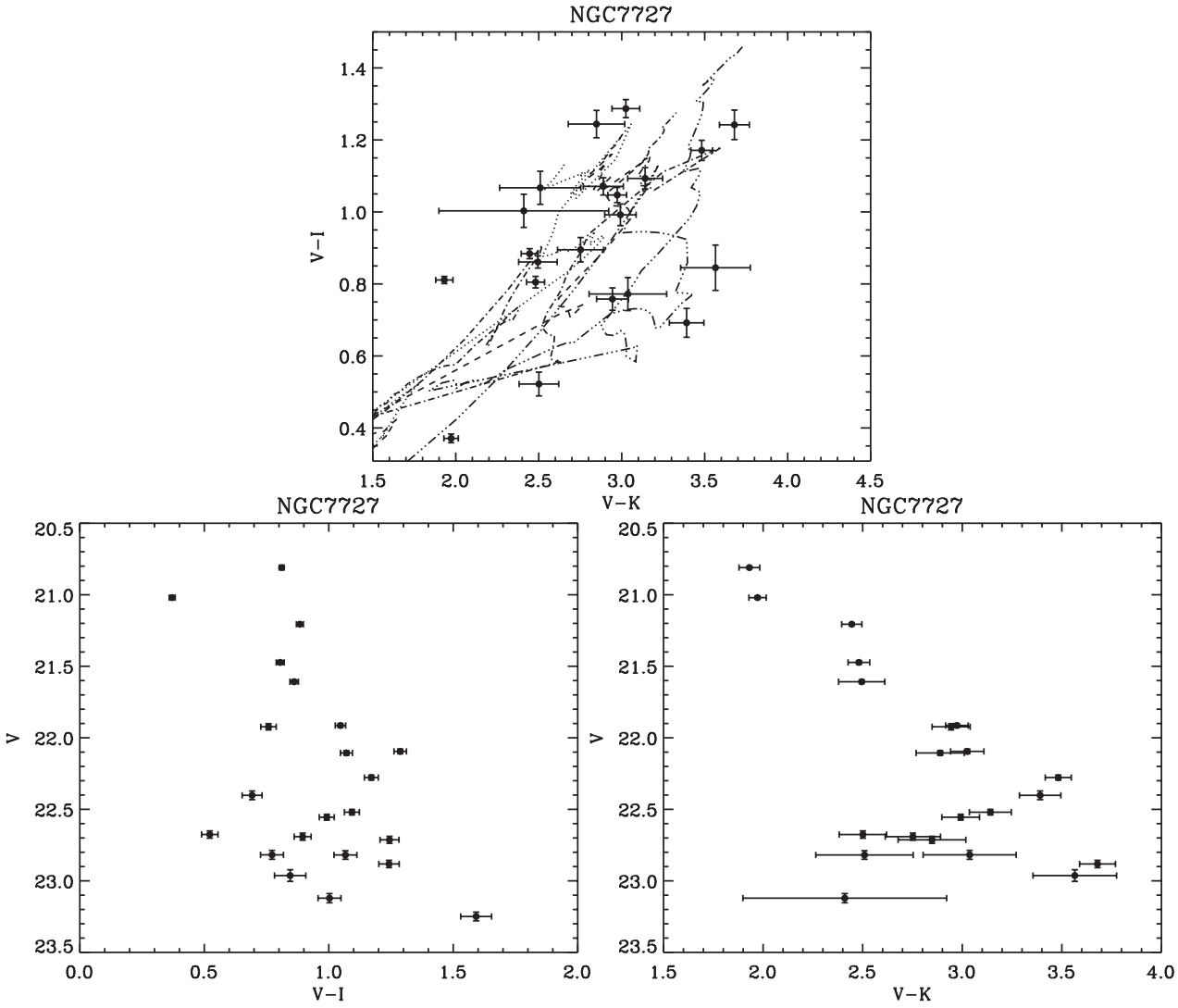

Figure 9. Color–magnitude and color–color diagrams for GCs of NGC 7727.

ies and is represented in our model simulations by clusters of mean logarithmic metallicity $[Z/Z_{\odot}] = -1.7$, with VIK_s colors computed by CB07; the size and age of this subpopulation is being held constant during the simulations for each galaxy. The two metal-rich subpopulations are assumed to both have logarithmic metallicities in the range of $-0.7 < [Z/Z_{\odot}] < 0.4$. The number ratios of metal-rich to metal-poor clusters, and of intermediate-age to old clusters within the metal-rich subpopulation, are then varied systematically.

With these assumptions made, the goal is to simulate the appearance of the mixed GC populations in $V-I$ vs $V-K_s$ diagrams with BC07 model clusters and to then compare these model diagrams with the observed diagrams for the GCs of each galaxy. The measure used for the comparison is provided by the cumulative age distributions of the artificial clusters and the observed GCs, both derived from the positions of the clusters in their respective $V-I$ vs $V-K_s$ diagrams and compared via a chi-squared (hereafter χ^2) test described below.

To *simulate* the observed mixed GC population of each galaxy, a set of model cluster $V-K_s$ colors was generated using a Monte Carlo technique. For each of the many simulations per galaxy, the total number of model clusters was made to equal the number of GC candidates in the galaxy (Table 3, last column). Corresponding model cluster $V-I$ colors were then computed based on the SSP models of CB07. To simulate observational errors, each model cluster population was furthermore convolved with photometric errors based on the indicative errors of our data. Finally, cumulative age distributions were calculated for each model cluster population, based on the same SSP models by CB07.

For each of our four galaxies, we generated a grid of 121 model cluster populations as follows. The age of the old metal-rich subpopulation was held fixed at 13 Gyr, while the age of the younger metal-rich subpopulation was set to 0.2, 0.5, 0.75, 1, 1.5, 2, 3, 5, 7, 10, and 13 Gyr. For each of these 11 ages, the ratio of young to old clusters was varied from 0% to 100% in 10% steps, thus yielding a total of 121 model populations for comparison with the observed GC population of each galaxy.

For each of the 121 age and number-ratio combinations, 1000 model samples were generated via the Monte Carlo technique, and the average cumulative age distribution (based on the SSP models) of the simulated clusters was calculated. The cumulative age distribution of the observed GCs was also calculated based on the same SSP models, via a transformation from the $V-I$ vs $V-K_s$ plane to the abundance vs log-age plane based on these models (for details, see Hempel & Kissler-Patig 2004).

We then performed χ^2 fitting of the model cumulative age distributions to the observed cumulative age distribution to determine which of the age and number-ratio combinations best fit the data. For each galaxy, a contour plot of the χ^2 values over the age vs. number-ratio configuration plane was drawn and used to infer the age and number ratio of the young metal-rich subpopulation as compared to the old subpopulation. These contour plots are shown and discussed in § 4.3 below.

4.2. *Verification of Technique*

In order to validate the use of this technique, we performed a series of verification tests independent from those performed by Hempel & Kissler-Patig (2004). Our verification method involved replacing the observed GC population with a simulated population of model clusters. The simulation of this population followed the same procedure as the simulations of our model populations described above.

First, we tested the ability of our adopted method to return an accurate value for the age of the younger metal-rich input population. As Figure 10 shows, while the age returned by the χ^2-fitting did not converge exactly to the simulated input age, it was largely consistent (to within $\sim$10%). Hence, we can confirm that, over the range of ages ($\sim 1-5$ Gyr) that we are investigating, the method returns a reasonably accurate age for a given input age.

Second, we also tested our method's stability with respect to the photometric errors of the input data. For a given age and ratio configuration, we varied the photometric errors from 0.1 mag to 0.3 mag. Note that (i) the indicative photometric errors in our observed data were below 0.3 mag, and (ii) while there were some clusters with higher errors, they were cut before the χ^2-fitting was performed.

Figure 11 highlights that, as expected, increasing the errors decreased the convergence of the χ^2 fit. Even so, however, the age returned by the fitting contours was still largely consistent with the simulated input age. Thus, we confirm the validity of our method for both the ages and the indicative photometric errors of the input data.

¿From the spread in the χ^2 contours and the deviation of the converged age from the input age we infer an upper limit for the age uncertainty of about $\pm$0.75 Gyr. Similarly, for the young-to-old ratio we find an upper limit to the uncertainty of about $\pm$20%. These uncertainties will be used for the GC subpopulations of each galaxy in the following sections.

4.3. *Cluster Ages*

Figure 12 shows contour plots of χ^2 values over the modeled configuration space for each GC system of our four sample galaxies. In each contour plot, the convergence of χ^2 to a minimum value marks the most likely

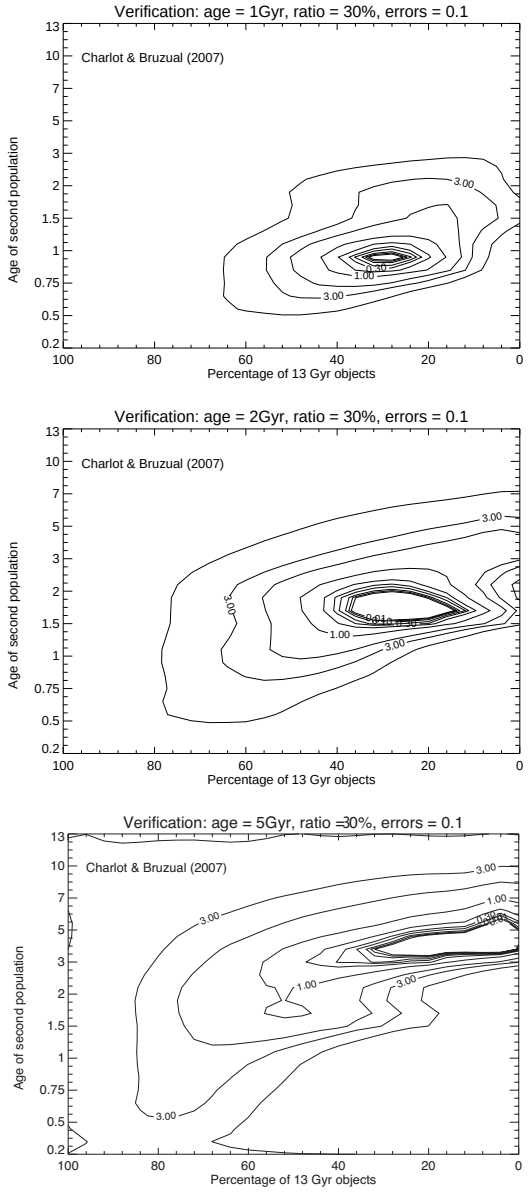
Verification: age = 1Gyr, ratio = 30%, errors = 0.1
Charlot & Bruzual (2007)
Age of second population
Percentage of 13 Gyr objects
Verification: age = 2Gyr, ratio = 30%, errors = 0.1
Charlot & Bruzual (2007)
Age of second population
Percentage of 13 Gyr objects
Verification: age = 5Gyr, ratio = 30%, errors = 0.1
Charlot & Bruzual (2007)
Age of second population
Percentage of 13 Gyr objects

Figure 10. χ^2 contour plots using a simulated cluster population as input. The age of the younger subpopulation increases from 1 Gyr (top) to 2 Gyr (middle) and 5 Gyr (bottom). The input age, number ratio, and photometric error are given for each.

combination of age and number-ratio for the younger GC subpopulation of that galaxy, based on the SSP models by CB07. Table 4 summarizes these resulting combinations, which we now briefly discuss for each galaxy.

4.3.1. *NGC 1700*

For this galaxy, Figure 12 shows that the χ^2 values converge to a minimum at a GC population mix consisting of about 5% of an old subpopulation and 95% of a younger subpopulation with an age of 1.7 ± 0.8 Gyr.

Note that this age is consistent with the previously published age estimate of 3 ± 1 Gyr (Brown et al. 2000) to within the combined errors. Note also that the quoted percentages apply only to the *observed* GC candidates, and not to the entire GC population, whose total number and subpopulation percentages are unknown.

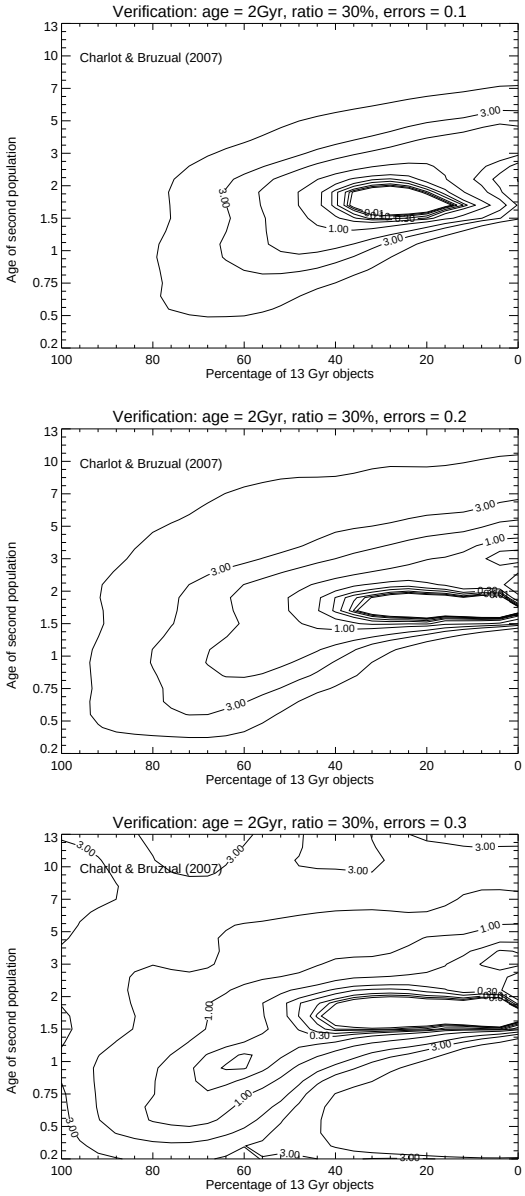
Verification: age = 2Gyr, ratio = 30%, errors = 0.1
Charlot & Bruzual (2007)
Age of second population
Percentage of 13 Gyr objects
Verification: age = 2Gyr, ratio = 30%, errors = 0.2
Charlot & Bruzual (2007)
Age of second population
Percentage of 13 Gyr objects
Verification: age = 2Gyr, ratio = 30%, errors = 0.3
Charlot & Bruzual (2007)
Age of second population
Percentage of 13 Gyr objects

Figure 11. χ^2 contour plots using a simulated cluster population as input. The size of the photometric errors increases from 0.1 mag (top) to 0.2 mag (middle) and 0.3 mag (bottom). The input age, number ratio, and photometric error are given for each.

4.3.2. *NGC 2865*

For NGC 2865, the χ^2 contours again show a high level of convergence, as can be seen in the top-right panel of Figure 12. From the contour minimum we infer a younger metal-rich GC subpopulation of age 1.8 ± 0.8 Gyr, comprising about 90% of the observed GC candidates.

Again, this newly determined age for the younger GCs compares well with the previously published age of 1.8 ± 0.5 Gyr for the young *stellar* subpopulation in this galaxy (Rampazzo et al. 2007).

4.3.3. *NGC 4382*

For NGC 4382, the χ^2 contours shown in Figure 12 indicate a younger metal-rich GC subpopulation of age 1.8 ± 0.8 Gyr, comprising between about 75% and 95% of the observed GC candidates.

Note that the χ^2 values for the GCs in NGC 4382 are much smaller than those for the GCs in the other three galaxies, suggesting a better agreement between the observed GC data and the simulated cluster populations.

As can be seen, there is also a significantly wider spread for the ratio of young-to-old GCs. Recall, however, that our primary interest is in the age of the younger subpopulation, and note that the convergence in age is very high. This newly determined age for the younger metal-rich GC subpopulation agrees well with the previously published age of 1.6 ± 0.3 Gyr for the young *stellar* subpopulation of this galaxy (Sansom et al. 2006).

4.3.4. *NGC 7727*

Finally, for NGC 7727 the χ^2 contours of Figure 12 indicate a purely young metal-rich GC population of age 0.9 ± 0.8 Gyr. The observed GC candidates of this galaxy are noteworthy both for their particularly young ages and for the apparent absence of an older subpopulation. Both of these characteristics were previously reported by Trancho et al. (2004), who obtained a GC population age of 1 – 2 Gyrs. Note, however, that the population of old metal-poor GCs universally present in all major galaxies may be too faint to be detected on our K_s-band images. Hence, its apparent absence may simply reflect a selection effect and does not imply that this old metal-poor GC population doesn't exist.

5. SUMMARY AND CONCLUSIONS

We have presented an age analysis of GC systems in four early-type galaxies that are considered candidate remnants of recent mergers. New K_s-band photometry of the GCs in these galaxies has been obtained with two near-infrared imagers on Gemini and combined with existing *HST* photometry in V and I to produce color–color and color–magnitude diagrams of the GC systems in VIK_s. These data have been fitted to simple toy models of mixed GC populations containing three subpopulations that differ in age and metallicity. The mixed GC populations have been simulated with SSP models by Charlot & Bruzual (2007, private communication) and compared to the observations. Various χ^2 fits to the cumulative age distributions derived from our data and from the toy models yield clear evidence for the presence of intermediate-age, metal-rich subpopulations of GCs in each of the four early-type galaxies. At the observed, relatively bright K_s magnitudes these intermediate-age subpopulations exceed the old metal-rich and metal-poor subpopulations in cluster numbers, and their estimated ages of $\sim 1 - 2$ Gyr are consistent with published ages for the same galaxies based on the integrated light. Thus, VIK_s photometry of GC populations in early-type galaxies can be used to date epochs of major star and cluster formation presumably due to relatively recent merger events.

We thank Stéphane Charlot and Gustavo Bruzual for sending us an early version of their new cluster-population models ("CB07"), presently still under development, and Maren Hempel and Markus Kissler-Patig for helpful information and a copy of their simulation code. We also thank the anonymous referee, whose

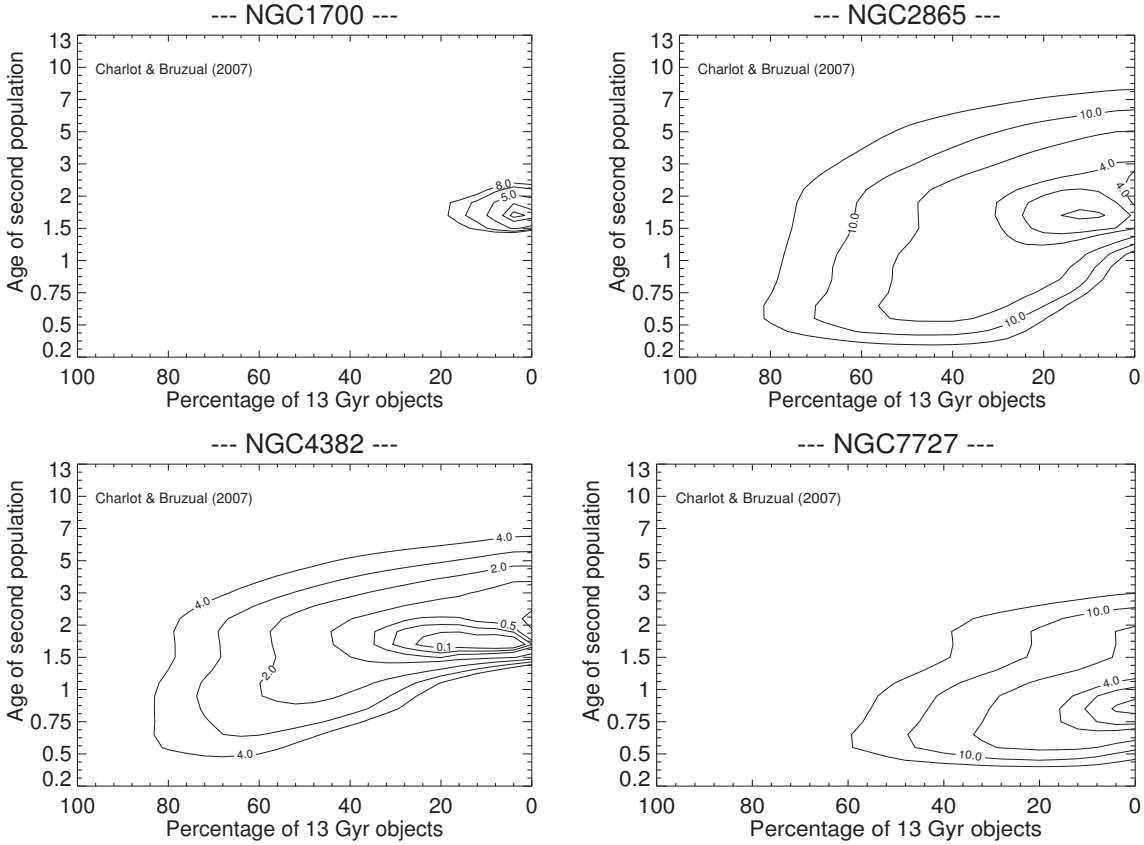

Figure 12. Contour plots of χ^2 values from fits of SSP model colors (CB07) to our VIK_s colors for GCs in NGC 1700, 2865, 4382, and 7727. Notice that the percentages of 13 Gyr old GCs among those observed are small. Most observed GCs in the four sample galaxies belong to younger, metal-rich subpopulations of intermediate age (see Table 4).

Table 4
Results of χ^2 fitting: Ages and percentages of intermediate-age GC subpopulations

Galaxy NGC	Age[a] (Gyr)	Percentage Young[b]	Published Age (Gyr)	Source
1700	1.7±0.8	95%	3 ± 1.0	Brown et al. (2000)
2865	1.8±0.8	90%	1.8 ± 0.5	Rampazzo et al. (2007)
4382	1.8±0.8	85%	1.6 ± 0.3	Sansom et al. (2006)
7727	0.9±0.8	100%	$1-2$	Trancho et al. (2004)

[a] Age of young metal-rich GC subpopulation as determined from χ^2 contours.
[b] Percentage of observed GC candidates belonging to the younger subpopulation as determined from χ^2 contours.

constructive comments helped us improve the presentation of our results. This research is based on observations obtained at the Gemini Observatory, which is operated by the Association of Universities for Research in Astronomy, Inc., under a cooperative agreement with the NSF on behalf of the Gemini partnership: the National Science Foundation (United States), the Particle Physics and Astronomy Research Council (United Kingdom), the National Research Council (Canada), CONICYT (Chile), the Australian Research Council (Australia), CNPq (Brazil) and CONICET (Argentina).

REFERENCES

Arp, H. 1966, Atlas of Peculiar Galaxies (Pasadena: California Institute of Technology); also: ApJS, 14, 1
Ashman, K. M., & Zepf, S. E. 1992, ApJ, 384, 50
Brown, R. J. N., Forbes, D. A., Kissler-Patig, M., & Brodie, J. P. 2000, MNRAS, 317, 406
Bruzual A., G. 2007, in ASP Conf. Proc. 374, From Stars to Galaxies: Building the Pieces to Build Up the Universe, ed. A. Vallenari et al. (San Francisco, CA: ASP), 303
Bruzual, G., & Charlot, S. 2003, MNRAS, 344, 1000
Crabtree, D. R., & Smecker-Hane, T. 1994, BAAS, 26, 1499
de Vaucouleurs, G., & de Vaucouleurs, A. 1964, Reference Catalogue of Bright Galaxies (Austin, TX: Univ. of Texas Press)
Elston, R., Raines, S. N., Hanna, K. T., et al. 2003, Proc. SPIEE, 4841, 1611
Fall, S. M., & Zhang, Q. 2001, ApJ, 561, 751
Fisher, D., Franx, M., & Illingworth, G. 1996, ApJ, 459, 110

Fleming, D. E. B., Harris, W. E., Pritchet, C. J., & Hanes, D. A. 1995, AJ, 109, 1044
Freedman, W. L., & Madore, B. F. 2010, ARA&A, 48, 673
Georgakakis, A., Forbes, D. A., & Norris, R. P. 2000, MNRAS, 318, 124
Harris, W. E. 1991, ARA&A, 29, 543
Hau, G. K. T., Carter, D., & Balcells, M. 1999, MNRAS, 306, 437
Hempel, M., & Kissler-Patig, M. 2004, A&A, 419, 863
Hodapp, K. W., Jensen, J. B., Irwin, E. M., et al. 2003, PASP, 115, 1388
Jordan, A., Peng, E. W., Blakeslee, J. P., et al. 2009, VizieR On-line Data Catalog; also: ApJS, 180, 54
Kissler-Patig, M. 2000, in ASP Conf. Ser. 211, Massive Stellar Clusters, ed. A. Lançon & C. Boily (San Francisco: ASP), 157
Kleineberg, K., Sánchez-Blázquez, P., & Vazdekis, A. 2011, ApJ, 732, L33
Kormendy, J., Fisher, D. B., Cornell, M. E., & Bender, R. 2009, ApJS, 182, 216
Lauer, T. R., Faber, S. M., Gebhardt, K., et al. 2005, AJ, 129, 2138
Malin, D. F., & Carter, D. 1983, ApJ, 274, 534
McDermid, R., Emsellem, E., Cappellari, M., et al. 2004, Astron. Nachr., 325, 100
Miller, B., Whitmore, B. C., Schweizer, F., & Fall, S. M. 1997, AJ, 114, 2381
Peng, E. W., Côté, P., Jordán, A., et al. 2006, ApJ, 639, 838
Puzia, T. H., Zepf, S. E., Kissler-Patig, M., et al. 2002, A&A, 391, 453
Rampazzo, R., Marino, A., Tantalo, R., et al. 2007, MNRAS, 381, 245
Sandage, A., & Tammann, G. A. 1981, A Revised Shapley-Ames Catalog of Bright Galaxies (Washington, DC: Carnegie Institution of Washington)
Sansom, A. E., O'Sullivan, E., Forbes, D. A., Proctor, R. N., & Davis, D. S. 2006, MNRAS, 370, 1541
Schiminovich, D., van Gorkom, J. H., van der Hulst, J. M., & Malin, D. F. 1995, ApJ, 444, L77
Schweizer, F. 1987, in Nearly Normal Galaxies, ed. S. M. Faber (Springer: New York), 18
Schweizer, F., & Seitzer, P. 1988, ApJ, 328, 88
Schweizer, F., Seitzer, P., Faber, S. M., et al. 1990, ApJ, 364, L33
Schweizer, F., & Seitzer, P. 1992, AJ, 104, 1039
Seitzer, P., & Schweizer, F. 1990, in Dynamics and Interactions of Galaxies, ed. R. Wielen (Berlin: Springer), 60
Serra, P., & Oosterloo, T. A. 2010, MNRAS, 401, L29
Sikkema, G., Peletier, R. F., Carter, D., Valentijn, E. A., & Balcells, M. 2006, A&A, 458, 53
Statler, T. S., Smecker-Hane, T., & Cecil, G. N. 1996, AJ, 111, 1512
Strader, J., Brodie, J. P., Schweizer, F., Larsen, S. S., & Seitzer, P. 2003, AJ, 125, 626
Trancho, G., Miller, B. W., Schweizer, F., & Whitmore, B. 2004, in ASP Conf. Ser. 322, The Formation and Evolution of Massive Young Star Clusters, ed. H. J. G. L. M. Lamers, L. J. Smith, & A. Nota (San Francisco: ASP), 219
Vorontsov-Velyaminov, B. A. 1959, Atlas and Catalog of Interacting Galaxies (Moscow: Sternberg Institute, Moscow State Univ.)
Whitmore, B. C., Schweizer, F., Leitherer, C., Borne, K., & Robert, C. 1993, AJ, 106, 1354
Whitmore, B. C., Miller, B. W., Schweizer, F., & Fall, S. M. 1997, AJ, 114, 1797
Worthey, G. 1999, in ASP Conf. Ser. 192, Spectrophotometric Dating of Stars and Galaxies, ed. I. Hubany, S. R. Heap, & R. H. Cornett (San Francisco: ASP), 283
Zepf, S. E., Ashman, K. M., English, J., Freeman, K. C., & Sharples, R. M. 1999, AJ, 118, 752